Large-eddy simulation of turbulent flow over spanwise-offset barchan dunes: Interdune vortex stretching drives asymmetric erosion

Chao Wang and William Anderson*
Mechanical Engineering Department, The University of Texas at Dallas, Richardson, Texas 75080, USA

(Received 7 July 2017; revised manuscript received 21 May 2018; published 18 September 2018)

The coupling between turbulent flow physics and barchan dune geometry is important to dune migration, morphology of individual dunes, and the morphodynamics of merging and separating proximal dunes. Large-eddy simulation was used to model turbulent, inertial-dominated flow over a series of static barchan dune configurations. The dune configurations were carefully designed to capture realistic stages of a so-called "offset interaction," wherein a small dune is placed upflow of a relatively larger dune, thereby guaranteeing interaction since the former migrates faster than the latter. Moreover, as interaction proceeds, the morphology of the small dune is mostly preserved, while the large dune undergoes dramatic transformation with greater erosion downflow of the interdune space. Simulations reveal that the wake centerline—determined here as the spanwise location at which the momentum deficit associated with each dune exhibits a minimum—veers due to dune geometry. Visualization of vortex identifiers reveals that hairpin vortices are produced via separation across the crestline of dunes, and these hairpins are advected downflow by the prevailing, background flow. The legs of hairpins emanating from the upflow dune contain streamwise vorticity of opposite sign, wherein the hairpin leg within the interdune space exhibits positive streamwise vorticity. This positive streamwise vorticity is supplied to the interdune space, where flow channeling induces acceleration of streamwise velocity. An assessment of right-hand side terms of the Reynolds-averaged streamwise vorticity transport equation confirm, indeed, that vortex stretching is the dominant contributor to sustenance of streamwise vorticity. With this, we can conclude that asymmetry of the large, downflow dune is a consequence of scour due to the interdune roller, and scouring intensifies as the spacing between dunes decreases. A structural model outlining this process is presented.

DOI: 10.1103/PhysRevE.98.033112

I. INTRODUCTION

The feedback between imposed aerodynamic and hydrodynamic loading and sand dune geometry is a control on sand dune morphology and the spatial migration rate of dunes [1–14], since sediment transport is the product of surface stress imposed by the above fluid. Under the inertial-dominated conditions typical of the atmospheric surface layer (ASL) [2,12,15,16] or the roughness sublayer of aquatic flows over river dunes [4], surface stress is dominated by turbulence [17] and, therefore, $\tau^w \sim u^2$, where τ^w is surface stress and u is the dominant component of the velocity vector, $\boldsymbol{u}$ [18]. Since sediment (saltation) mass flux, q, scales nonlinearly with shear velocity, $q \sim u_*^n$, and because $\tau^w \sim u_*^2 \sim u^2$, it follows that $q \sim u^n$ [1,19–21]. Although specific values for scaling exponent, n, vary, $n = 3$ is commonly cited [20,21], which demonstrates the extent to which dune morphodynamics are influenced by turbulent fluctuations. Some very recent studies have reported stronger support for $n = 2$, but this still demonstrates the importance if turbulent fluctuations [22,23]. In this work, large-eddy simulation (LES) has been used to model flow over a stages of a dune interaction; rigorous assessment of turbulent processes responsible for sustenance of vortical flow structures—and their role in advancing the interaction—have been performed. Note that in this work, the flow is assumed to be incompressible, and thus flow quantities are considered on a density-normalized basis. In the interest of generality, therefore, we will refer to the "upflow" and "downflow" direction throughout [12,24].

A. Background

Dune morphology is controlled by a range of parameters [25], or boundary conditions, although for the present article we focus on prevailing flow direction (other factors, including soil moisture and vegetation, can stabilize dunes and alter their geometry, but such influences are not considered for this study). Variability in wind direction—whether associated with local processes, or with processes occurring over diurnal, seasonal, or larger-scale climatic oscillations—alters barchan dune morphology and can result in crescentic, linear, or star dunes [1,2,26–29]. Under the action of a unidirectional flow, canonical barchan dunes in isolation form and migrate in the downflow direction [30,31]. The prevailing flow direction is coaligned with the x axis (in this article, the first, second, and third component of any vector corresponds with its value in the streamwise, spanwise, and vertical direction, respectively, including the Euclidian vector, $\boldsymbol{x} = \{x, y, z\}$). Isolated barchans are defined by centerline symmetry about the streamwise-vertical plane, with limbs of sediment extending in the downflow direction, but symmetry rapidly breaks down with even modest flow variability [32]. Herein, we

*wca140030@utdallas.edu

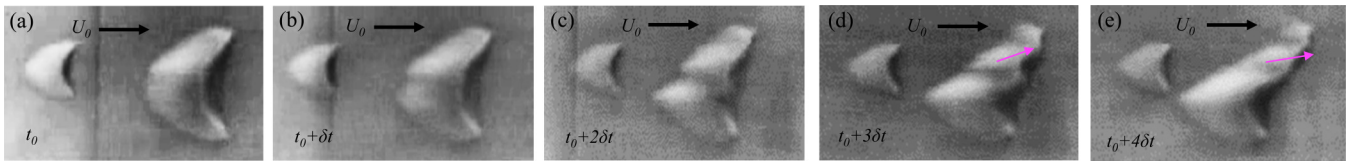

FIG. 1. Photographs of offset merger interaction stages [26], observed in mobile-bed flume experiments (images retrieved from Hersen and Douady [31]). Annotations of prevailing mean flow direction and representative times added for illustration; red arrows illustrate downflow trajectory of ejected dune, or the "ejecta" [25].

focus on morphodynamic changes associated with local flow variability due to the presence of proximal dunes.

Dune migration is the product of cumulative grain transport, with individual grains saltating over the windward (stoss) side before careering down the lee side via avalanche. It follows, then, that the migration rate is inversely proportional to dune volume, $\mathcal{V} = \int_{\mathcal{A}} h(\boldsymbol{x}) d^2\boldsymbol{x}$, where $\mathcal{A}$ and $h(\boldsymbol{x})$ is the x-y plane and digital elevation model of an individual dune, respectively. Thus, for a field composed of a spectrum of dune sizes, the preceding volume-migration proportionality argument demonstrates that dunes are likely to collide, or interact, as the trajectory of smaller and larger dunes overlap [26,27,33]. Aloft and downflow of individual dunes, the flow is greatly perturbed by individual dunes (this is true of the mean, or Reynolds-averaged flow, and fluctuations superimposed upon the Reynolds average). Thus, in the context of the driving flow, dune interactions are likely to begin long before dune junctions occur.

Owing to the number of parameters affecting dune morphodynamics, and the capacity for parameters to vary in space and time, natural dune fields exhibit geometric complexity over a range of scales [25]. Large-scale computer simulation of flow over a dune field—i.e., one with spatial extent in the horizontal direction many times larger than the depth of the aloft flow—would present a substantial computational challenge. Indeed, Khosronejad and Sotiropoulos (2014) [13] recently used a coupled morphodynamic solver to dynamically capture key aspects of dune genesis, evolution, and dune field self organization [34–39]; their results agreed favorably with flume results from Venditti *et al.* [40–43]. For the present work, however, we focused on a building-block interaction, which exists as part of a larger set of canonical interactions [26]: the offset merger interaction. We have used a series of high-fidelity diagnostic techniques to explain how, and why, this interaction advances.

Figure 1 shows instantaneous photographs of an offset merger interaction, recorded during flume experiments by Hersen and Douady (2005) [31]. For these images, a unidirectional flow induces migration of a relatively small and large barchan, where the former is placed upflow of the latter, thereby guaranteeing interaction. As time advances, the small dune approaches the large dune, while morphology of the former exhibits no discernible time dependence. The larger downflow dune, however, undergoes a major transformation as time advances. The horn of the downflow dune coaligned with the trajectory of the upflow dune is elongated, with the dune becoming more asymmetric as the upflow spacing diminishes (the term "horn" is used to denote the lateral extremities of barchan dunes).

B. Prior work

In a preceding article [24], we considered four static dune topographies inspired by the Fig. 1 series. In that study, experimental measurements and LES runs were used to highlight the presence of a channeling flow in the interdune space between the upflow and downflow dune. Analysis of the mean flow resulted in illustration that the wake of the upflow and downflow dunes is not coaligned with the streamwise direction, but instead veers. This was referred to as "wake veering": the wake veering profiles between experiments and simulations agreed closely, and we reported a trend of monotonically increasing spanwise veering of wakes as dune spacing decreases [discussion to follow in text accompanying Figs. 4(g) and 4(h)].

In our previous study [24], the large downflow dune was symmetric about the centerline for all four cases, though Fig. 1 shows that this is an incorrect depiction of the morphological realizations exhibited as an actual offset-merger interaction advances [14]. Moreover, we did not determine the *driving mechanism* responsible for the flow channeling. That is: what processes in the interdune space are responsible for sustenance of the channeling, and why do these processes intensify as proximal dune spacing declines?

With these questions, six static dune configurations have been considered for the present article. The configurations were carefully selected to mimic stages from the series of photographs in Fig. 1, and are illustrated in Fig. 2. Comprehensive discussion of the cases is provided below, but here we mention a few key attributes. First, Case S1 features an isolated barchan, which serves as a basis for comparison against Cases S2 to S4 [Fig. 2(a)]. Cases S3′ and S4′, shown in Figs. 2(b) and 2(c), respectively, feature an asymmetric large downflow dune with small upflow dune at declining streamwise spacing. On Fig. 2(a), annotations of the spanwise offset, s_y/h, and streamwise offset, s_x/h, are shown, while the level of asymmetry, $\Delta x/h$, is sketched on Figs. 2(b) and 2(c). The inclusion of Cases S3′ and S4′ provides far greater generality by virtue of the asymmetry, $\Delta x/h$, that is a clear manifestation of the offset merger interaction (Fig. 1). Cases S5 and S6 are high-resolution versions of S2 and S4, respectively, and are included to demonstrate that the simulations are not affected by resolution. Since no resolution sensitivity is reported for these cases, we declined to assess resolution sensitivity for other cases.

C. This study

LES has been used to model inertial-dominated flow over the cases depicted in Fig. 2. This work is an extension of

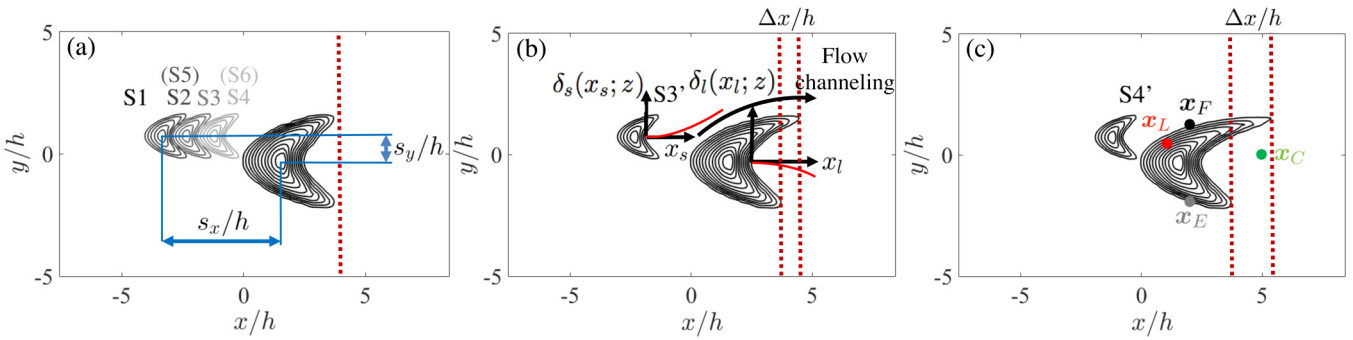

FIG. 2. Visualization of dune configurations considered for this study. Panel (a) shows Cases S1 to S4, Panel (b) shows Case S3′, and Panel (c) shows Case S4′ (see Table I for summary of simulation and geometric attributes). For visualization purposes, streamwise and spanwise position have been normalized by large dune crest height, h. Panel (a) includes annotation of streamwise offset, s_x/h, spanwise offset, s_y/h, and streamwise asymmetry, $\Delta x/h$. Cases S3′ and S4′ are equivalent to S3 and S4, respectively, with the exception of $\Delta x/h$ streamwise asymmetry. Recall Fig. 1, which shows how the large downflow dune horn exhibits asymmetric elongation as the upflow dune approaches [38], which is why we have considered S3′ and S4′. In all cases (except S1), the upflow dune is equivalent, and a ratio of the small dune volume is computed and provided in Table I, where $\chi = \mathcal{V}_s/\mathcal{V}_L$, and where $\mathcal{V}_s$ and $\mathcal{V}_L$ is the volume associated with the small and large dune, respectively. Panel (b) annotations show local coordinates, x_s and x_l, used to quantify dune wakes, $\delta_s(x_s;z)$ and $\delta_l(x_l;z)$ (red lines). Solid black arrow denotes flow channeling. Panel (c) shows discrete locations (solid circles) used for time-series sampling of flow quantities, where $\boldsymbol{x}_L/h = \{1, 0.5, 0.5\}$, $\boldsymbol{x}_C/h = \{5, 0, 0.5\}$, $\boldsymbol{x}_E/h = \{2, -2, z/h\}$, and $\boldsymbol{x}_F/h = \{2, 1.3, z/h\}$. Table I gives detailed attributes of each case. Note, finally, that the small dune crest height is denoted by h_s. Individual dune digital elevation models provided by K. Christensen, Notre Dame, and used in recent articles [11,14,24].

the findings from our previous article [24], but herein we have used post-processing tools to fully elucidate the driving mechanisms responsible for the morphodynamics observed in Fig. 1; moreover, we consider additional cases that capture the actual spatial asymmetry exhibited by the large downflow dune.

In Sec. II, we present the LES code, while in Sec. III we provide comprehensive description of the dune cases. In Sec. IV, results directly retrieved from the simulations (and derived from rigorous post processing) are presented. The results culminate in presentation of a model for flow structures within the interdune space and explanation of their role in driving the asymmetric morphology of the large, downflow dune. Specifically, we demonstrate that streamwise vorticity embodied within the legs of hairpins shed from the small dune are supplied to the interdune space—where flow channeling forces a streamwise gradient in streamwise velocity—which yields vortex stretching and sustains the interdune roller. Concluding remarks are provided in Sec. V.

We must emphasize that the present study considers static dunes, and the simulations include no sediment-fluid morphodynamic coupling. In recent times, others have made major contributions in this area: for example, consider the work of Ortiz and Smolarkiewicz [44] or, more recently, Khosronejad and Sotiropoulos [13], where the former group modeled morphodynamic evolution of a barchan under unidirectional flow, while the latter group predicted evolution of an actual dune field. As opposed to Khosronejad and Sotiropoulos [13], who considered evolution of a field of dunes, in this article we adopted a "building block" approach, choosing instead to discern driving mechanisms responsible for one interaction. This approach is nonetheless relevant since, to our knowledge, detailed assessment of mechanisms driving the interdune rollers—which, as will be shown, are paramount during the interaction—has not been performed.

II. LARGE-EDDY SIMULATION

During LES, the three-dimensional transport equation for grid-filtered, incompressible momentum is solved: $D_t\tilde{\boldsymbol{u}}(\boldsymbol{x},t) = \boldsymbol{f}(\boldsymbol{x},t)$, where $\boldsymbol{f}(\boldsymbol{x},t)$ is a collection of forces (pressure correction, pressure gradient, stress heterogeneity, and obstacle forces), and $\tilde{\cdot}$ denotes a grid-filtered quantity. The grid-filtering operation is attained here via convolution with the spatial filtering kernel, $\tilde{\boldsymbol{u}}(\boldsymbol{x},t) = G_\Delta \star \boldsymbol{u}(\boldsymbol{x},t)$, where Δ is the filter scale [45]. The grid-filtering operation yields a right-hand side forcing term, $-\boldsymbol{\nabla}\cdot\mathbf{T}$, where $\mathbf{T} = \langle \boldsymbol{u}' \otimes \boldsymbol{u}' \rangle_t$ is the subgrid-scale stress tensor and $\langle . \rangle_a$ denotes averaging over dimension, a (in this article, rank-1 and -2 tensors are denoted with bold-italic and bold-sans relief, respectively).

For the present study, $D_t\tilde{\boldsymbol{u}}(\boldsymbol{x},t) = \boldsymbol{f}(\boldsymbol{x},t)$ is solved for a channel-flow arrangement [12,46], with the flow forced by a pressure gradient, $\boldsymbol{\Pi} = \{\Pi, 0, 0\}$, where $\Pi = [dP_0/dx]\frac{H}{\rho} = \tau^w/\rho = u_*^2 = 1$, which sets the shear velocity, u_*, upon which all velocities are scaled (H is the surface layer depth and τ^w is surface stress). $D_t\tilde{\boldsymbol{u}}(\boldsymbol{x},t) = \boldsymbol{f}(\boldsymbol{x},t)$ is solved for high-Reynolds number, fully rough conditions [18], and thus, $\nu\nabla^2\tilde{\boldsymbol{u}}(\boldsymbol{x},t) = 0$. Under the presumption of $\rho(\boldsymbol{x},t) \to \rho$, the velocity vector is solenoidal, $\boldsymbol{\nabla}\cdot\tilde{\boldsymbol{u}}(\boldsymbol{x},t) = 0$. During LES, the (dynamic) pressure needed to preserve $\boldsymbol{\nabla}\cdot\tilde{\boldsymbol{u}}(\boldsymbol{x},t) = 0$ is computed by computation of $\boldsymbol{\nabla}\cdot[D_t\tilde{\boldsymbol{u}}(\boldsymbol{x},t) = \boldsymbol{f}(\boldsymbol{x},t)]$ and imposing $\boldsymbol{\nabla}\cdot\tilde{\boldsymbol{u}}(\boldsymbol{x},t) = 0$, which yields a resultant pressure Poisson equation.

The channel-flow configuration is created by the aforementioned pressure-gradient forcing, and the following boundary condition prescription: at the domain top, the zero-stress Neumann boundary condition is imposed on streamwise and spanwise velocity, $\partial\tilde{u}/\partial z|_{z/H=1} = \partial\tilde{v}/\partial z|_{z/H=1} = 0$. The zero vertical velocity condition is imposed at the domain top and bottom, $\tilde{w}(x,y,z/H=0) = \tilde{w}(x,y,z/H=1) = 0$. Spectral discretization is used in the horizontal directions,

TABLE I. Summary of simulation attributes ($H = 100$ m, $u_{*,d} = 0.45\,\mathrm{m.s^{-1}}$) and dune field configurations considered for present article.

Case	N_x	N_y	N_z	L_x/H	L_y/H	L_z/H	$\hat{z}_0/H$	$\delta_t u_{*,d} H^{-1}$	TU_0/H	h/H	s_x/h	s_y/h	χ[a]	$\Delta x/h$
S1	128	128	128	4	4	1	1×10^{-5}	4.5×10^{-5}	1820.7	0.25	0.0	0.0	0.125	0.0
S2	128	128	128	4	4	1	1×10^{-5}	4.5×10^{-5}	1765.4	0.25	5.0	1.3	0.125	0.0
S3	128	128	128	4	4	1	1×10^{-5}	4.5×10^{-5}	1767.4	0.25	4.0	1.3	0.125	0.0
S4	128	128	128	4	4	1	1×10^{-5}	4.5×10^{-5}	1770.0	0.25	3.0	1.3	0.125	0.0
S3′	128	128	128	4	4	1	1×10^{-5}	4.5×10^{-5}	1769.9	0.25	4.0	1.3	0.125	1.0
S4′	128	128	128	4	4	1	1×10^{-5}	4.5×10^{-5}	1764.5	0.25	3.0	1.3	0.125	2.0
S5	256	256	256	4	4	1	1×10^{-5}	2.25×10^{-5}	1532.2	0.25	5.0	1.3	0.125	0.0
S6	256	256	256	4	4	1	1×10^{-5}	2.25×10^{-5}	1541.0	0.25	3.0	1.3	0.125	0.0

[a]Volume ratio, $\chi = \mathcal{V}_s/\mathcal{V}_L$, where $\mathcal{V}_s$ and $\mathcal{V}_s$ is volume of small and large dune, respectively.

thus imposing periodic boundary conditions on the vertical "faces" of the domain. The code uses a staggered-grid formulation [46], where the first grid points for $\tilde{u}(\boldsymbol{x}, t)$ and $\tilde{v}(\boldsymbol{x}, t)$ are located at $\delta z/2$, where $\delta z = H/N_z$ is the resolution of the computational mesh in the vertical (N_z is the number of vertical grid points). Grid resolution in the streamwise and spanwise direction is $\delta x = L_x/N_x$ and $\delta y = L_y/N_y$, respectively, where L and N denote horizontal domain extent and corresponding number of grid points, respectively (subscript x or y denotes streamwise or spanwise direction, respectively). Table I provides a summary of the domain attributes for the different cases, where the domain height has been set to the depth of the surface layer, $L_z/H = 1$.

At the lower boundary, surface momentum fluxes are prescribed with a hybrid scheme leveraging an immersed-boundary method (IBM) [47,48] and the equilibrium logarithmic model [49], depending on the digital elevation model, $h(x, y)$. When $h(x, y) < \delta z/2$, the topography is vertically unresolved, and the logarithmic law is used:

$$\tau_{xz}^{w}(x, y, t) = -\left[\frac{\kappa U(x, y, t)}{\log\left(\frac{1}{2}\delta z/\hat{z}_0\right)}\right]^2 \frac{\bar{\tilde{u}}\left(x, y, \frac{1}{2}\delta z, t\right)}{U(x, y, t)} \quad (1)$$

and

$$\tau_{yz}^{w}(x, y, t) = -\left[\frac{\kappa U(x, y, t)}{\log\left(\frac{1}{2}\delta z/\hat{z}_0\right)}\right]^2 \frac{\bar{\tilde{v}}\left(x, y, \frac{1}{2}\delta z, t\right)}{U(x, y, t)}, \quad (2)$$

where $\hat{z}_0/H = 1 \times 10^{-5}$ is a prescribed roughness length (summarized in Table I), $\bar{\tilde{}}$ denotes test-filtering [50,51] (used here to attenuate unphysical local surface stress fluctuations associated with localized application of Eqs (1) and (2) [52]), and $U(x, y, \frac{1}{2}\delta z, t) = (\bar{\tilde{u}}(x, y, \frac{1}{2}\delta z, t)^2 + \bar{\tilde{v}}(x, y, \frac{1}{2}\delta z, t)^2)^{1/2}$ is magnitude of the horizontal components of the test-filtered velocity vector. Wherever $h(x, y) > \frac{1}{2}\delta z$, a continuous forcing IBM is used [48,53], which has been successfully used in similar studies of turbulent obstructed shear flows [12,54,55]. The IBM computes a body force, $\boldsymbol{f}(\boldsymbol{x}, t)$, which imposes circumferential momentum fluxes at computational "cut" cells based on spatial gradients of $h(x, y)$. Equations (1) and (2) are needed to ensure surface stress is imposed when $h(x, y) < \frac{1}{2}\delta z$. Subgrid-scale stresses are modeled with an eddy-viscosity model, $\boldsymbol{\tau}^d = -2\nu_t \mathbf{S}$, where $\mathbf{S} = \frac{1}{2}(\nabla\tilde{\boldsymbol{u}} + \nabla\tilde{\boldsymbol{u}}^{\mathrm{T}})$ is the resolved strain-rate tensor. The eddy viscosity is $\nu_t = (C_s\Delta)^2|\mathbf{S}|$, where $|\mathbf{S}| = (2\mathbf{S} : \mathbf{S})^{1/2}$, C_s is the Smagorinsky coefficient, and Δ is the grid resolution. For the present simulations, the Lagrangian scale-dependent dynamic model is used [52] to assess C_s during LES. The simulations have been run for $N_t\delta_t U_0 u_{*,d} H^{-1} \approx 10^3$ large-eddy turnovers, where $U_0 = \langle\tilde{u}(x, y, (L_z - \delta z/2)/H = 1, t)\rangle_t$ is a "freestream" or centerline velocity. This duration is sufficient for computation of Reynolds-averaged quantities (specific values are reported in Table I).

Note that the $u_{*,d}$ and H cited in Table I are used only to normalize the dimensional time, $\delta t^* = \delta t u_* H^{-1}$. For all other purposes, flow quantities are normalized by the LES friction velocity, u_*, which is derived by the imposed (and nondimensional) pressure gradient, as per the text at the opening of this section. Owing to this approach, and due to the inertial-dominated state attained under fully rough flow conditions, the LES-derived flow statistics will exhibit dynamic similarity with flows in the atmospheric surface layer, the roughness sublayer of hydraulic flows, or laboratory flows in flumes or wind tunnels.

III. CASES

Cases S1 to S4 are shown in Fig. 2(a), Case S3′ is shown in Fig. 2(b), and Case S4′ is shown in Fig. 2(c). Cases S5 and S6 have identical topographic attributes to Cases S2 and S4, respectively, but are projected upon a relatively higher-resolution computational mesh (see Table I for simulation details). Cases S5 and S6 are included for the purpose of resolution sensitivity assessment; results confirm that computational resolution has no discernible effect on the results. For Cases S1 to S4, S5, and S6, the topographies are composed of streamwise-symmetric dunes, where Case S1 is a single isolated dune. For Cases S2 to S4, S5, and S6, the large central dune from Case S1 is retained, and an additional small dune is placed at a series of upflow locations, s_x/h, from a spanwise-offset position, s_y/h, where h is the crest height of the large dune (for perspective, horizontal position is normalized by h for Fig. 2 and subsequent figures). Note that the streamwise and spanwise offsets are recorded in Table I. Note also that for Fig. 2 and subsequent figures, we have shifted the coordinate origin to the farthest upflow point of the large dune (colloquially referred to as the "toe"), which helps to visualize the digital elevation models and flow fields.

The topographic configurations are intended to capture instantaneous morphodynamic realizations of an actual offset-merger interaction, though Fig. 1 shows that the large dune changes profoundly as the smaller upflow dune approaches.

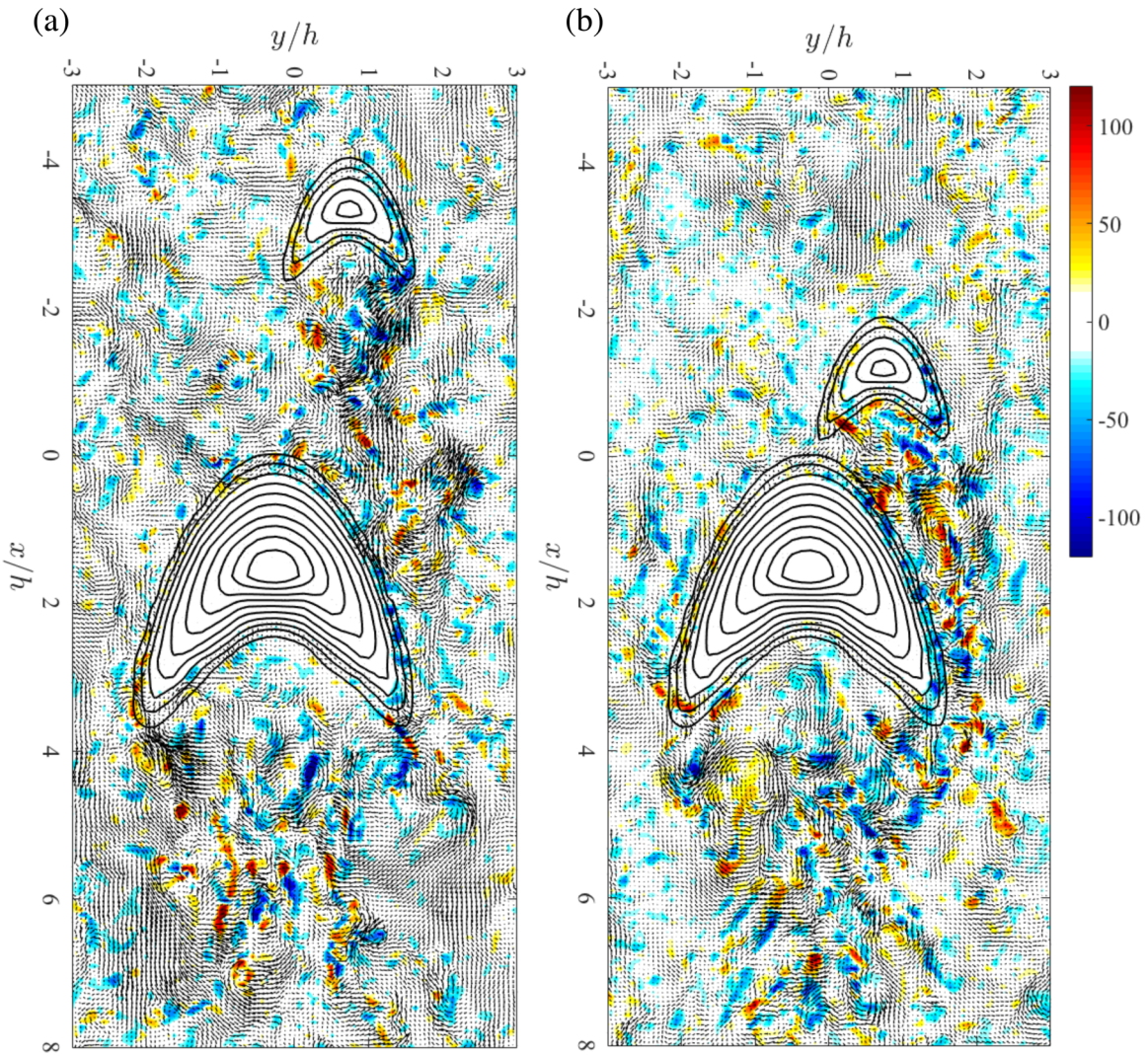

FIG. 3. Streamwise-spanwise plane visualization of instantaneous flow over Cases S5 (a) and S6 (b) (see Table I for topography details). Visualization shown at wall-normal elevation, $z/h = 0.25$. Contour and vectors are swirl strength with sign set by out-of-plane vorticity, $\lambda^*_{c,z}(x, y, z/h = 0.25, t) = \lambda_c(x, y, z/h = 0.25, t)\hat{i}_{\omega,z}(x, y, z/h = 0.25, t)$, and instantaneous fluctuating velocity, $\{\tilde{u}'(x, y, z/h = 0.25, t)/u_*, \tilde{v}'(x, y, z/h = 0.25, t)/u_*\}$, respectively.

For this reason, two additional cases—S3′ [Fig. 2(b)] and S4′ [Fig. 2(c)]—are considered, wherein the large downflow dune exhibits the spanwise asymmetry that is characteristic of this particular interaction. The level of asymmetry is quantified by parameter, Δx, and is annotated on Figs. 2(b) and 2(c) (since Cases S1–S4 correspond with a symmetric dune, $\Delta x = 0$ for these cases). By using high-fidelity LES to model turbulent flow over these cases, we can study flow physics aloft the dunes and explain why the dune interaction advances as observed in Fig. 1.

For Cases S2–S4, S3′, and S4′, the height of the small dune is precisely half the height of the larger downflow dune. For perspective, we construct the volumetric ratio, $\chi = \mathcal{V}_s/\mathcal{V}_L = \int_{\mathcal{A}_s} h(\boldsymbol{x})d^2\boldsymbol{x} / \int_{\mathcal{A}_L} h(\boldsymbol{x})d^2\boldsymbol{x}$, where subscripts "$s$" and "$L$" denote small and large dune, respectively. For all the cases considered in this article, $\chi = 1/8$. Note that, to an extent not considered here, Cases S1–S4 were considered in our recent article [24]. But, in the present work, we have considered additional cases that match actual morphodynamic realizations—S3′ and S4′—and we perform in-depth post-processing analyses that provide deeper insights into the aero- and hydrodynamic processes sustaining this interaction.

Note that the annotations on Fig. 2(b)—x_s, $\delta_s(x_s; z)$, x_l, and $\delta_l(x_l; z)$—relate to the so-called wake-veering phenomenon, which was presented in our previous article [24], but will be revisited in Sec. IV for Cases S3′ and S4′ (this panel includes annotation of the interdune "flow channeling," the importance of which will be revealed in Sec. IV D). The discrete locations shown on Fig. 2(b) ($\boldsymbol{x}_L$, $\boldsymbol{x}_C$, $\boldsymbol{x}_E$, and $\boldsymbol{x}_F$) are used in Sec. IV C to record time series of velocity and probability density functions (PDF; discussion to follow).

The dune DEMs were provided by Ken Christensen, Notre Dame, based on experimental work on turbulent flow over barchan dunes in their refractive-index matched facility [11,14]. The DEMs were, themselves, originally derived from Hersen *et al.* [30]. Thus, attributes of the dunes have been carefully tuned to replicate natural morphological states realized by actual dunes in nature.

IV. RESULTS

This section is composed of four subsections, which are used to systematically demonstrate how turbulence responds to dunes and why the offset-merger interaction advances through the instantaneous realizations captured in Fig. 1. The results will be used to demonstrate that asymmetry of the large, downflow dune is driven by a persistent interdune roller. Vorticity dynamics reveal that sustenance of the roller is overwhelmingly derived from vortex stretching mechanism: positive streamwise vorticity within the interdune space is supplied by hairpin vortices, which are exposed to a channeling flow with positive streamwise velocity gradient.

A. Instantaneous and Reynolds-averaged flow: Channeling and wake veering

Figure 3 shows instantaneous visualization of fluctuating streamwise-spanwise velocity (vectors) and swirl strength, signed here by the unit vector for vorticity, $\hat{\boldsymbol{i}}_\omega = \tilde{\boldsymbol{\omega}}/|\tilde{\boldsymbol{\omega}}| = \tilde{\omega}_x/|\tilde{\boldsymbol{\omega}}|\hat{i} + \tilde{\omega}_y/|\tilde{\boldsymbol{\omega}}|\hat{j} + \tilde{\omega}_z/|\tilde{\boldsymbol{\omega}}|\hat{k}$ [56]. Thus, swirl strength is a vector quantity, $\boldsymbol{\lambda}_c^* = \lambda_c \hat{\boldsymbol{i}}_\omega$. For the purpose of Fig. 3, the color flood contour shows $\lambda_{c,z}^*$. Vortical activity is concentrated within the wake regions of all dunes, where the local regions of $\lambda_{c,z}^* > 0$ and $\lambda_{c,z}^* < 0$ are indicators of the legs of hairpins originating from the dune crests (additional results shown in Fig. 5). In the interdune space [i.e., $-3 \lesssim x/H \lesssim 1$ and $0 \lesssim y/h \lesssim 2$ on Fig. 3(a)], it is apparent that the small dune wake veers in conformance with the large dune geometry. This is apparent also in Fig. 3(b). In this article, we contend that wake veering from the small dune is responsible for the large dune asymmetry.

Figures 4(a)–4(f) show contours of Reynolds-averaged vertical vorticity, where $\langle\tilde{\omega}_z\rangle_t = \partial_x\langle\tilde{v}\rangle_t - \partial_y\langle\tilde{u}\rangle_t \approx -\partial_y\langle\tilde{u}\rangle_t$, since the magnitude of spanwise heterogeneities must greatly exceed the magnitude of streamwise heterogeneities by virtue of the wake shear [24]. Thus, $\langle\tilde{\omega}_z\rangle_t$ is a marker of wake shear intensity. The contours reveal $\langle\tilde{\omega}_z\rangle_t > 0$ and $\langle\tilde{\omega}_z\rangle_t < 0$ in the wakes emanating from the "bottom" and "top" horns, respectively, where application of the right-hand rule confirms the efficacy of this result. For completeness, we show the low-pass filtered wake centerline, found here via location of points with $\langle\tilde{\omega}_z\rangle_t(\boldsymbol{x}) = 0$ [where datapoints downflow of the small and large dune will be denoted with $\delta_s(x_s; z)$ and $\delta_l(x_l; z)$, respectively, and where x_s and x_l are the origins of local coordinate systems; see Fig. 2(b)].

For Case S1, the $\langle\tilde{\omega}_z\rangle_t$ contours are roughly equal and opposite, and the wake centerline is virtually horizontal, which is to be expected for an isolated obstacle. However, the addition of the spanwise-staggered small upflow dune entirely disrupts this flow pattern. Indeed, for Case S2, the small dune wake veers through the interdune space, while the distribution of $\langle\tilde{\omega}_z\rangle_t$ in the vicinity of the large dune is asymmetric. The zone of maximum $|\langle\tilde{\omega}_z\rangle_t|$ on the "top" and "bottom" side of the large dune is rotated, where the negative (blue) and positive (red) zones have migrated upflow and downflow, respectively. In the interest of consistency, we adopted equivalent colorbar limits for the six panels, and we point out that the lower limit (negative) of the colorbar is roughly three times the magnitude of the upper limit (positive). The large negative values are concentrated on the "top" face of the downflow dune, and are developed as the flow is forced to channel through the interdune space. This result can be discerned, too, from inspection of the wake profiles, which even for Case S2 [maximum s_x/h, Fig. 4(h)] exhibits a distinct veering, relative to Case S1.

As the spacing decreases for Cases S3 and S4 [Figs. 4(c) and 4(d)], asymmetry in $\langle\tilde{\omega}_z\rangle_t$ becomes more pronounced. Elevated $|\langle\tilde{\omega}_z\rangle_t|$ across the large dune stoss face can be viewed as a proxy for surface stress, and the relatively larger values over the "top" region (i.e., $y/h > 0$ and $x/h > 0$) are responsible for asymmetric morphology of the downflow dune (also observed in the flume experiments; Fig. 1). At the elevation considered in Fig. 4, $z/h = 0.5$, the small dune wake is far more sensitive to changing attributes of the topography, relative to the large dune. Recall, however, that the small dune height is equivalent to $z/h = 0.5$, and when the same contours are generated at $z/h = 1$, the large dune wake responds more to s_x/h, etc., but we have excluded these figures here for brevity.

For Cases S3′ and S4′ [Figs. 4(e) and 4(f)], the small dune wakes are further perturbed, and yet the only difference between these and Cases S3 and S4 is asymmetry of the large dune. Note, however, a subtle but important difference in the $\langle\tilde{\omega}_z\rangle_t$ distributions for Cases S3 and S3′ [Figs. 4(c) and 4(e)], and for Cases S4 and S4′ [Figs. 4(d) and 4(f)]: for the "prime" cases, the region of $\langle\tilde{\omega}_z\rangle_t > 0$ (red) and $\langle\tilde{\omega}_z\rangle_t < 0$ (blue) is larger and smaller, respectively. Since the small dune forces elevated flow through the interdune space, the asymmetric dunes provide a larger area over which momentum fluxes can occur (i.e., drag), and this helps to attenuate flow asymmetry.

We have recorded the wake profiles from Figs. 4(a) to 4(f) and compiled them on Figs. 4(g) and 4(h), which show $\delta_s(x_s; z/h = 0.5)/h$ and $\delta_l(x_l; z/h = 0.5)/h$, respectively (see Fig. 2 for graphical details of local coordinate system and wake profiles). As per the caption, the black, gray, and light gray profiles correspond with Cases S2, S3, and S4, respectively, and it is thus apparent that wake veering intensifies monotonically with decreasing s_x/h (this is true in the wake of the small and large dune). Furthermore, comparing the wakes for S3 and S3′ (gray and dashed blue), $\delta_s(x_s; z)/h$ is similar between the two cases while $\delta_l(x_l; z)/h$ is substantially smaller for the asymmetric dune. For Cases S4 and S4′ (light gray and dotted red), $\delta_s(x_s; z)/h$ is, again, similar for the small dune but smaller for the large asymmetric dune. This is attributed to the aforementioned weakening asymmetry in $\langle\tilde{\omega}_z\rangle_t$ for Cases S3′ and S4′, where the larger frontal area helps to absorb momentum on the face of the large dune exposed to the interdune channeling flow. The cyan circles and dash-dot magenta line correspond with S5 and S6, respectively, and exhibit close agreement with the black and light gray profiles (S2 and S4). This serves as evidence of resolution insensitivity.

With the results presented in this section, we have established that asymmetry of the wakes is directly related to geometric attributes of the dunes. In the following section, we study the three-dimensional nature of flow processes proximal to the dunes using vortex identification and conditional sampling. We conditionally sample the flow based upon exceedence of a low-probability, high-magnitude event, which

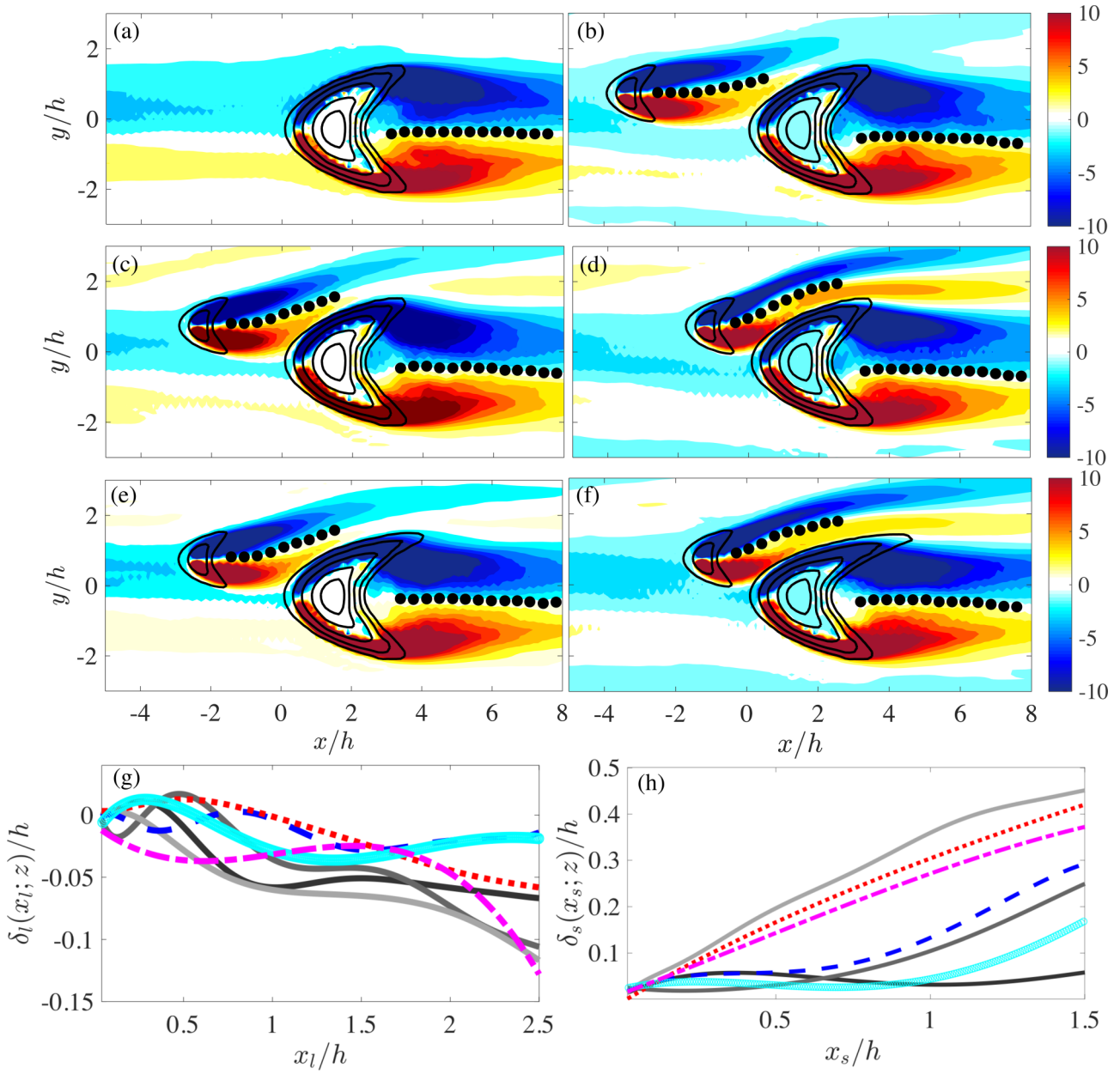

FIG. 4. Color flood contour of Reynolds-averaged vertical vorticity, $\langle\tilde{\omega}_z\rangle_t(x, y, z/h = 0.5)$, at wall-normal elevation, $z/h = 0.5$, for Cases S1 (a); S2 (b); S3 (c); S4 (d); S3′ (e); and S4′ (f) (see Table I for topography details). Included on the color floods are low-pass filtered datapoints for the wake, emanating from the small and large dunes, $\delta_s(x_s; z/h = 0.5)$ and $\delta_l(x_l; z/h = 0.5)$, respectively. Low-pass filtered wake profiles emanating from large and small dunes, $\delta_l(x_l; z/h = 0.5)$ (Panel g) and $\delta_s(x_s; z/h = 0.5)$ (Panel h), respectively, where local coordinate originates at respective dune crest, where Fig. 2 graphically illustrates the local axes, x_s and x_l. Black, gray, and light gray solid lines correspond with Cases S2, S3, and S4, respectively, dashed blue and dotted red lines correspond with S3′ and S4′, respectively, while cyan circles and dash-dot magenta line correspond with S5 and S6, respectively.

is especially relevant to aeolian systems since sediment mass fluxes scale nonlinearly upon ambient surface stress (which is set by turbulent fluctuations). Using wavelet decomposition, we will also demonstrate that vortices proximal to the dunes are a direct product of shedding from the dunes.

B. Vortex shedding and wavelet analysis

This section addresses two complementary aspects of flow in the interdune space. First, we present visualization of a vortex identifier derived from both the conditionally averaged and instantaneous flow [57–61]. Since saltation mass fluxes are heavily influenced by intermittent fluctuations in imposed surface stress, it is important to consider flow attributes during extreme conditions [62–64]. This exercise confirms the existence of hairpin vortices being shed from the dune crests, which are forced to undergo downflow advection (in a subsequent section, we will demonstrate that streamwise vorticity originating within the hairpin legs is intrinsically important to large dune asymmetry). Given the importance of hairpin

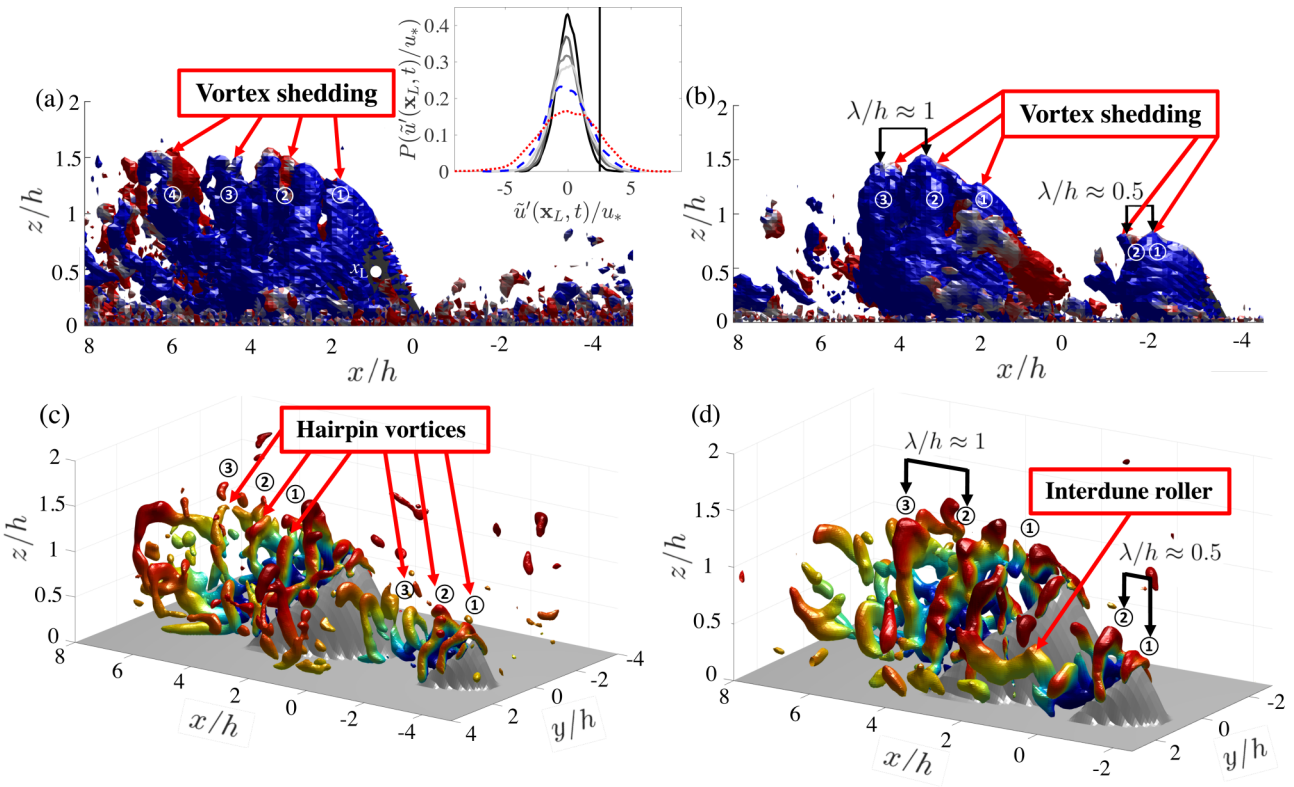

FIG. 5. Streamwise–wall-normal visualization of conditionally-averaged Q criterion for $\widehat{Q} = 11$ signed by conditionally-averaged wall-normal rotating direction: Panels (a) and (b) show Cases S1 and S2, respectively. Probability density function (PDF) of normalized streamwise velocity fluctuation at sampling position $\boldsymbol{x} = \boldsymbol{x}_L$ is showed in panel (a). Black, dark gray, gray, and light gray lines correspond with Cases S1, S2, S3, and S4, respectively, while dashed blue and dotted red datapoints correspond with S3′ and S4′, respectively (see Table I and Fig. 2 for topography details). Black vertical line notes the conditional sampling threshold used in this work is $\tilde{u}'(\boldsymbol{x}_L,t)/u_* > 2.5$ [57–64]. Three-dimensional visualization of instantaneous Q criterion for $Q = 100$ signed by Reynolds-averaged streamwise velocity: Panels (c) and (d) show Cases S5 and S6, respectively. Note numbered annotation of successive vortex cores emanating from dune brinkline, and vortex core spacing, δ_s/h, deduced from high-Reynolds number Strouhal number and advective velocity in vicinity of brinkline.

structures upon the morphodynamics, wavelet decomposition has been performed. The result confirms that the vortices are produced at a dominant frequency directly associated with the dune attributes.

Figure 2(c) shows Case S4′ with annotations for discrete sampling locations, $\boldsymbol{x}_L$, $\boldsymbol{x}_C$, $\boldsymbol{x}_F$, and $\boldsymbol{x}_E$ (see caption for additional information on discrete points). Flow statistics at these discrete locations are presumed to capture influences of the dune configurations. Here, we focus specifically on position $\boldsymbol{x}_L/h = \{1.0, 0.5, 0.5\}$, at which the influence of flow channeling, separation from the small dune, and changing dune topographic configurations are especially pronounced.

Time-series recording of $\tilde{u}'(\boldsymbol{x}_L,t)/u_*$, over $\sim\mathcal{O}(10^3)$ large-eddy turnovers have been used to generate the PDF shown in Fig. 5(a, inset). The PDFs exhibit wide, or heavy, tails that are the signature of intermittent, high-magnitude events. Moreover, the PDFs contain rich information about how upflow disturbances due to the relatively smaller dune can profoundly alter the statistics at downflow points. Since the mean flow has been subtracted before generating the PDFs, the PDFs are all centered around 0 (this facilitates intercomparison between the cases). First, the PDFs exhibit clear widening for Cases S1 to S4, which is due to the diminishing s_x/h, for which the wake effects due to the small dune are closer to the sampling point. Note, too, that the PDFs for Cases S3′ (dashed blue) and S4′ (dotted red) exhibit yet wider PDFs, and, thus, the probability of the mean is least for these cases.

For discussion, consider the existence of a site at which the prevailing winds cannot develop a Reynolds-averaged u_* capable of exceeding the threshold needed to mobilize sediment, $u_{*,t}$ [1,19–21] (in the context of aeolian processes on Earth, such conditions could occur due to seasonal meteorological variability). However, the PDFs in Fig. 5(a) show that u_*—which is set by fluctuations in the aloft flow—could greatly exceed its average over brief periods of time. In a related article, Chinthaka and Anderson [64] recently used LES to reveal the spatial attributes of flow structures in the atmospheric boundary layer during brief, high-magnitude values of u_*, and showed how coherent structures within the atmospheric surface layer could induce stresses substantially exceeding the average.

For the present article, we used the threshold, $\tilde{u}'(\boldsymbol{x}_L,t)/u_* > 2.5$, which has been added as an annotation on Fig. 5(a, inset). Since the PDFs all exhibit different distributions, the resultant conditionally-averaged statistics do not correspond with an event likely to occur with the same probability. It is apparent, however, that in all cases we have sampled the flow based on events with a 5 to 15% probability of occurrence.

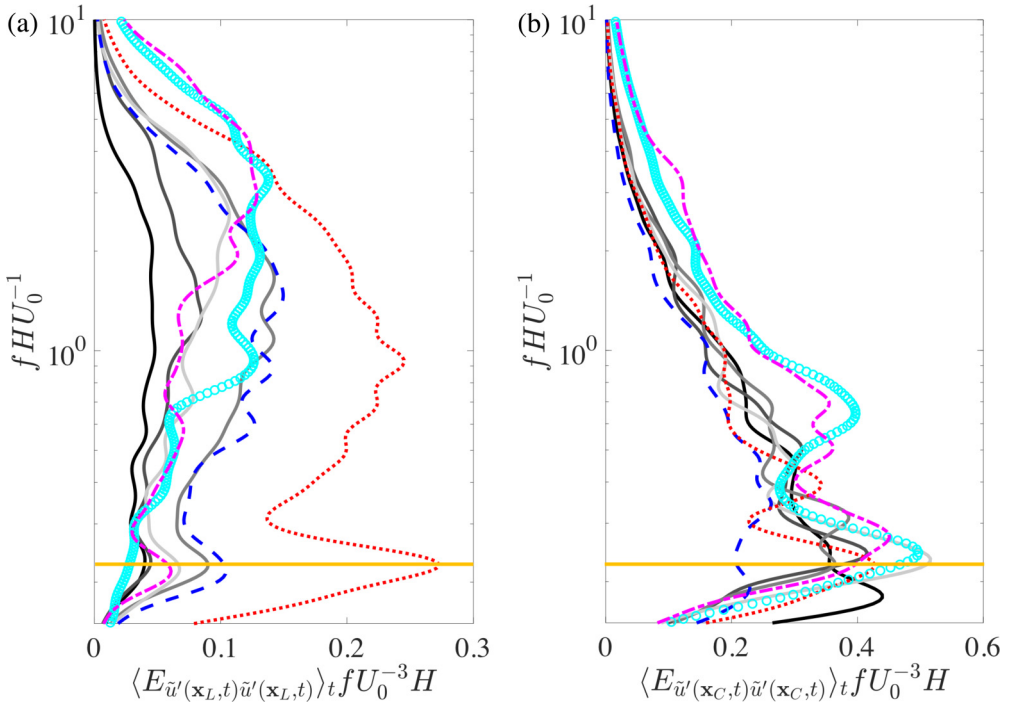

FIG. 6. Global wavelet power spectrum of streamwise velocity fluctuations, for input time series from discrete locations $\boldsymbol{x}_L$ (a) and $\boldsymbol{x}_C$ (b). Black, dark gray, gray, and light gray lines correspond with Cases S1, S2, S3, and S4, respectively, dashed blue and dotted red lines correspond with S3′ and S4′, respectively, while cyan circles and dash-dot magenta line correspond with S5 and S6, respectively. Horizontal orange line denotes $fHU_0^{-1} = St = 0.25$, the high-Reynolds number asymptote.

After computation of the PDF and selection of the threshold, we then run the LES for an additional period of time and sample the flow based on

$$\frac{\widehat{\tilde{\boldsymbol{u}}}(\boldsymbol{x})}{u_*} = \left\langle \frac{\tilde{\boldsymbol{u}}(\boldsymbol{x},t)}{u_*} \middle| \frac{\tilde{u}'(\boldsymbol{x}_L,t)}{u_*} > 2.5 \right\rangle_{N_s}, \tag{3}$$

where $\widehat{\ldots}$ denotes a conditionally-averaged quantity, and N_s is the number of times $\tilde{u}'(\boldsymbol{x}_L,t)/u_* > 2.5$. Having conditionally sampled the flow with Eq. (3), we compute the Q criterion vortex identifier, which is derived from the velocity gradient tensor, $\mathbf{D} = \nabla\tilde{\boldsymbol{u}}$ [65–67]. $\mathbf{D}$ can be decomposed into its symmetric and anti-symmetric components, $\mathbf{D} = \mathbf{S} + \boldsymbol{\Omega}$, where $\mathbf{S} = \frac{1}{2}(\nabla\tilde{\boldsymbol{u}} - \nabla\tilde{\boldsymbol{u}}^{\mathrm{T}})$ and $\boldsymbol{\Omega} = \frac{1}{2}(\nabla\tilde{\boldsymbol{u}} + \nabla\tilde{\boldsymbol{u}}^{\mathrm{T}})$, allowing computation of the Q criterion with

$$Q = \frac{1}{2}(\boldsymbol{\Omega} : \boldsymbol{\Omega} - \mathbf{S} : \mathbf{S}). \tag{4}$$

Figures 5(a) and 5(b) show isosurfaces of conditionally averaged Q criterion for Cases S1 and S2, respectively, in the streamwise–wall-normal plane (see Fig. 5(a) inset for conditional sampling threshold). These figures reveal the presence of a train of vortex cores, migrating downflow following separation at the crest (for Case S1, we have annotated vortex cores 1 to 4, while for Case S2, we have annotated vortex cores in the wake of the large and small dune). Figures 5(c) and 5(d) show three-dimensional isosurfaces of instantaneous Q criterion for high-resolution cases, S5 and S6, respectively. Compared with the conditionally-averaged visualizations, instantaneously-sampled three-dimensional fields from the high-resolution cases are relatively less organized. Nonetheless, there is a discernible pattern of hairpin-like structures emanating downflow of both dunes, while one of the cases has captured the interdune roller [Fig. 5(d)]. The interdune roller, we will show, is foremost in setting the asymmetric topology of the larger dune. The structure of successive hairpin heads resembles observations from canonical wall turbulence [67,68].

To explain the downflow spacing between successive vortex cores annotated in Fig. 5, we have used global wavelet power spectrum. Wavelet decomposition is a convenient tool for illustrating the spectral density of input time series in joint time-frequency space [69,70]. Global wavelet power spectrum profiles are attained via convolution of an input time series with a spectrum of wavelet functions, computation of spectral density (wavelet power spectrum contour), and averaging over time at each distinct frequency (global wavelet power spectrum profile). This procedure is useful in the detection of energetic peaks associated with vortex shedding downflow of the large dune. For the present analysis, we consider $\tilde{u}(\boldsymbol{x}_L,t)$ and $\tilde{u}(\boldsymbol{x}_C,t)$, discrete locations roughly upflow and downflow of the large dune, respectively [see Fig. 2(c)]. The analysis is predicated upon convolution of $\tilde{u}'(\boldsymbol{x},t)$ with a wavelet (basis) function, $\psi(f)$, which yields an array of coefficients in joint time-frequency space. The square of the absolute value of the wavelet coefficients, divided by each frequency, yields spectral density defined in time-frequency space, $E_{\tilde{u}'\tilde{u}'}(\boldsymbol{x},t)fU_0^{-3}H$, otherwise known as wavelet power spectrum contours. For the present work, we have used Morlet wavelets, $\psi(t/t_s) = \exp(i\omega_\psi t/t_s)\exp(|t/t_s|^2\frac{1}{2})$, where we have chosen the relatively common nondimensional frequency, $|\omega_\psi| = 6$, for which t_s is the wavelet timescale, t is physical time, and i is the imaginary unit.

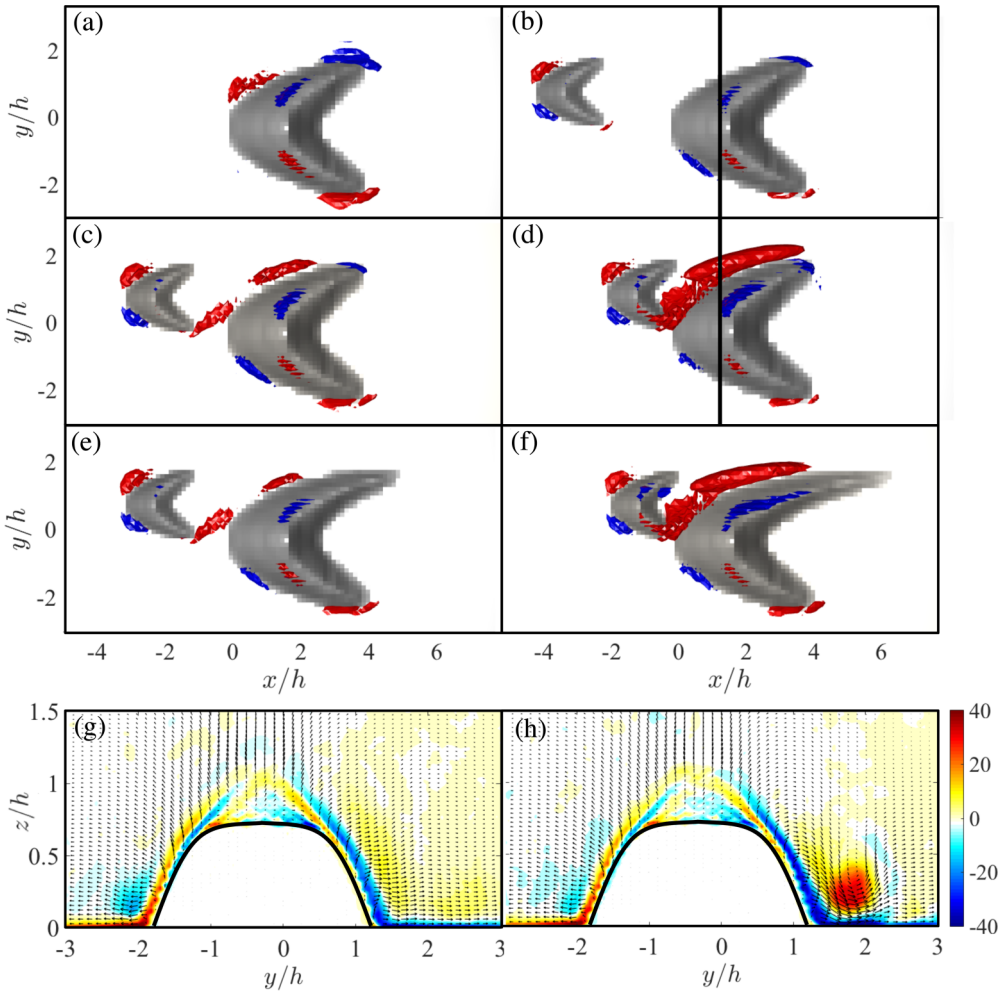

FIG. 7. Isosurface image of Reynolds-averaged, shear-normalized differential helicity, $h(\boldsymbol{x})Hu_*^{-2} = 120$ (red) and $h(\boldsymbol{x})Hu_*^{-2} = -120$ (blue). Panels (a) to (f) correspond with Cases S1, S2, S3, S4, S3′, and S4′, respectively. Panel (g) and (h) are Reynolds-averaged flow over S5 (g) and S6 (h) in spanwise-wall normal plane at $x/h = 1.7$, which are showed as black lines in panels (b) and (d), respectively (see Fig. 2 for reference). In panels (g) and (h), contour and vectors are Reynolds-averaged streamwise vorticity, $\langle\tilde{\omega}_x(\boldsymbol{x})\rangle_t$, and components of in-plane velocity, $\{\langle\tilde{v}(\boldsymbol{x},t)\rangle_t, \langle\tilde{w}(\boldsymbol{x})\rangle_t\}$.

Figure 6 shows global wavelet power spectrum profiles for the input time series denoted in the figure caption, $\langle E_{\tilde{u}'\tilde{u}'}(\boldsymbol{x},t)\rangle_t fU_0^{-3}H$. Frequency has been shear normalized for the present purposes, where the ordinate label is equivalent to Strouhal number, $St = fHU_0^{-1}$, where U_0 is Reynolds-averaged streamwise outer velocity (i.e., $U_0 = \langle\tilde{u}(x, y, z/H = 1, t)\rangle_{x,y,t}$. For high-Reynolds number flows, such as the present, Strouhal number tends toward an asymptotic value, $St \approx 0.25$, which has been denoted by the horizontal orange line on Fig. 6. For Case S1 at location $\boldsymbol{x}_L$, there is no distinct peak in any component of velocity. Instead, energy is distributed across constituent frequencies, due to the presence of channel-like turbulence upflow of the large dune (centered around a peak at $fHU_0^{-1} \approx 1$, a characteristic large-eddy timescale). However, the addition of the smaller upflow dune changes the spectral densities significantly.

Indeed, at position $\boldsymbol{x}_L$, the spectral densities of streamwise velocity fluctuation reveal the emergence of a second peak at $fHU_0^{-1} \approx 0.25$, which is the marker of vortex shedding from the upflow dune. As the streamwise spacing decreases, the energy associated with vortex shedding increases, and this is true for all cases. In contrast, at position $\boldsymbol{x}_C$, all input time series are affected by vortex shedding (including Case S1). Figure 6(b) reveals that the vortex shedding peak is the dominant energy-containing frequency, and visual inspection of Fig. 2 shows this to be a logical result given the proximity of $\boldsymbol{x}_C$ to the crest of the large dune. Note, too, that the profiles for Cases S2 and S4 are similar (profile and magnitude) to the profiles for S5 and S6, respectively, providing further evidence of resolution insensitivity in the LES code (color coding summarized in the figure caption).

Since Fig. 6 has revealed a distinct energetic peak associated with vortex shedding at $St = fHU_0^{-1} = 0.25$, we can return now to Fig. 5 and the streamwise spacing between successive vortex cores. For the purposes of an estimation, we presume that the advective velocity of each vortex core is U_0, which can be related to the distance between successive hairpin vortices, λ, via $U_0 = \lambda f$. With this, $U_0 = \lambda StU_0/H$, which can be rearranged to $\lambda = StH$. Put differently, we can normalize by the dune height, yielding $\lambda/h \approx 1$ and $\lambda/h \approx \frac{1}{2}$ for the large and small dune, respectively. Annotations for

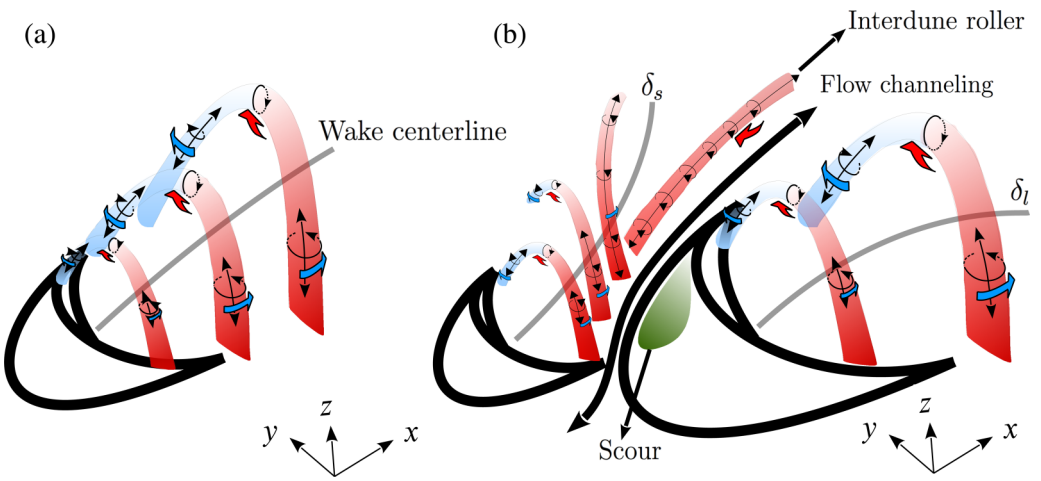

FIG. 8. Structural model for flow processes associated with dune morphodynamic asymmetry. Panel (a): idealized hairpin vortices shed from dune brinkline; Panel (b): idealized hairpin vortices being simultaneously shed from both dunes, where streamwise vorticity embodied within inner leg of upflow hairpin is stretched by flow channeling (double-headed roller), sustaining the interdune roller and inducing sediment scour on the large dune (green). Red and blue colors denote positive and negative streamwise vorticity directions, respectively [see Figs. 5(c) and 5(d) for three-dimensional instantaneous visualization]. On both panels, gray lines denote dune wake centerline (see also Figs. 2 and 4 for details).

this spacing have been added to Fig. 5. Inspection of Fig. 5 shows that this exercise yields perfectly consistent predictions on the vortex core spacing, and confirms that vortical activity proximal to the dunes originates via separation from the dune crests.

C. Sediment scour and asymmetric erosion

In this section, we will further elaborate on the significance of the interdune roller in the context of dune morphodynamics. First, we will illustrate the existence of the interdune roller through introduction of differential helicity—a quantity that defaults to zero in the absence of simultaneous, coaligned velocity and vorticity. In the present context, helicity is ideal for studying the interdune roller since its presence highlights both the channeling flow and streamwise vorticity. We will conclude that this constitutes a "channel-and-scour" mechanism, and show that this mechanism explains the pronounced asymmetry of the large dune during offset interaction (Fig. 2). With this, a structural model is presented to summarize how hairpins shed from the upflow dune introduce streamwise vorticity, and how this streamwise vorticity drives asymmetric erosion across the large dune.

Reynolds-averaged, differential helicity is computed as the inner product of velocity and vorticity:

$$H_l = \int \langle \tilde{\boldsymbol{\omega}}(\boldsymbol{x},t)\cdot\tilde{\boldsymbol{u}}(\boldsymbol{x},t)\rangle_t d^3\boldsymbol{x}, \tag{5}$$

where $d^3\boldsymbol{x}$ is the volume over which H_l is to be computed. For the present purposes, it is more convenient to consider differential helicity,

$$h_l(\boldsymbol{x}) = \frac{dH_l}{d^3\boldsymbol{x}} = \langle \tilde{\boldsymbol{\omega}}(\boldsymbol{x},t)\cdot\tilde{\boldsymbol{u}}(\boldsymbol{x},t)\rangle_t. \tag{6}$$

In the absence of coalignment between the velocity and vorticity vectors, helicity vanishes. In the context of the interdune roller, differential helicity [as per Eq. (6)] is interesting since it reveals the presence of any accompanying advection. This is relevant to dune morphodynamics, since it implies that the interdune roller scours sediment from the large dune while simultaneously inducing net downflow transport. Figures 7(a)–7(f) shows isosurfaces of $h_l(\boldsymbol{x})$, as per Eq. (6).

It is apparent, firstly, that the $h_l(\boldsymbol{x})$ distribution is roughly symmetric for Case S1 [Fig. 7(a)]. However, even for Case S2 (largest s_x/h), the $h_l(\boldsymbol{x})$ distribution is entirely modified. As the upflow dune approaches the larger downflow dune [Cases S3 and S4, Figs. 5(c) and 5(d)], the spatial extent of the advecting interdune roller increases. The $h_l(\boldsymbol{x})$ isosurface is actually smaller for Cases S3′ and S4′, which is consistent with preceding results on attenuation of flow asymmetry (i.e., Figs. 6 and 8) for the asymmetric dune cases. We clarify, finally, that streamwise vorticity and velocity make the dominant contribution to helicity, i.e., $h_l(\boldsymbol{x}) \approx \tilde{\omega}_x(\boldsymbol{x})\tilde{u}(\boldsymbol{x})$. Thus, the isosurfaces are true markers of a roller undergoing persistent advection through the interdune space.

To demonstrate the importance of the interdune roller for sediment scour from the large dune, and thus morphodynamic asymmetry, Figs. 7(g) and 7(h) show spanwise–wall-normal visualization of Reynolds-averaged streamwise vorticity for Cases S5 [Fig. 7(g)] and S6 [Fig. 7(h)], where the y-z plane positions have been denoted as solid black lines on Figs. 7(b) and 7(d), respectively. The signature of the interdune roller is captured in the red region of $\langle\tilde{\omega}_x(\boldsymbol{x})\rangle_t$, while the vector field shows how the roller induces scour down the face of the large dune (while channeling through the interdune space transports sediment downflow, advancing the interaction and enforcing morphodynamic asymmetry).

For completeness, Fig. 8 is an idealized sketch of these process for an isolated [Fig. 8(a)] and offset interaction [Fig. 8(b)] configuration. For the isolated case, we have sketched production of a succession of idealized hairpins [7,9,10,12,13,71], which migrate downflow (supporting instantaneous and quantitative supporting results of this were reviewed in Sec. IV B).

For the offset interaction case, however, the picture changes significantly. Here, self-similar hairpins are produced via separation at the small dune crest. The hairpins are colored by streamwise vorticity, which explains how separation from the small dune serves as the source of streamwise vorticity. Upon production, this streamwise vorticity is subjected to immediate stretching due to the channeling flow (this section). As a result, a persistent interdune roller is present in the interdune space—confirmed, also, with visualization of differential helicity—and this roller scours sediment from the inner face of the large dune [Fig. 8(b)]. Sediment eroded by the roller is transported downflow before being deposited, which explains the asymmetry exhibited by the large dune as the interaction proceeds. The sketch also provides annotations of the wake veering profiles, which were reviewed in Sec. IV A.

The results in this section have highlighted the simultaneous importance of the interdune channeling flow and its rotational sign. We argue that the interdune roller scours sediment from the large dune, and that this is foremost in setting the dune morphology as interaction advances. To close the argument, we present results of vorticity budgeting in the following section. Results demonstrate that, indeed, stretching of ambient streamwise vorticity provides the largest gain to streamwise vorticity in the interdune space.

D. Turbulent vorticity dynamics

As a final post-processing measure, we have used the Reynolds-averaged velocity and total stresses to elucidate mechanisms responsible for sustaining the interdune roller. Consider, first, the Reynolds-averaged incompressible momentum transport equation:

$$\frac{1}{2}\boldsymbol{\nabla}(\langle\tilde{\boldsymbol{u}}\rangle_t\cdot\langle\tilde{\boldsymbol{u}}\rangle_t)-\langle\tilde{\boldsymbol{u}}\rangle_t\times\langle\tilde{\boldsymbol{\omega}}\rangle_t=-\frac{1}{\rho}\boldsymbol{\nabla}\tilde{p}-\boldsymbol{\nabla}\cdot\langle\mathbf{T}\rangle_t+\boldsymbol{\Pi}+\boldsymbol{f}, \tag{7}$$

where $\mathbf{T}=\langle\boldsymbol{u}'\otimes\boldsymbol{u}'\rangle_t=\langle\tilde{\boldsymbol{u}}'\otimes\tilde{\boldsymbol{u}}'\rangle_t+\langle\boldsymbol{\tau}\rangle_t$, where the first and second right-hand side terms are the resolved and subgrid-scale stress tensor (this additive approach is necessary when assembling the total stresses from LES datasets *a posteriori*); $\boldsymbol{f}$ represents imposed forces associated with the presence of solid obstacles via an IBM (see also Sec. II), while $\boldsymbol{\Pi}$ denotes any ambient pressure-gradient forcing. The transport equation for $\langle\tilde{\boldsymbol{\omega}}\rangle_t$ is derived via the curl of Eq. (7), yielding

$$\underbrace{\langle\tilde{\boldsymbol{u}}\rangle_t\cdot\boldsymbol{\nabla}\langle\tilde{\boldsymbol{\omega}}\rangle_t}_{\text{Advection}}=\underbrace{\langle\tilde{\boldsymbol{\omega}}\rangle_t\cdot\boldsymbol{\nabla}\langle\tilde{\boldsymbol{u}}\rangle_t}_{\text{Stretching and Tilting}}\underbrace{-\boldsymbol{\nabla}\times\boldsymbol{\nabla}\cdot\langle\mathbf{T}\rangle_t}_{\text{Turbulent torque}}, \tag{8}$$

where annotations have been used to denote the stretching and tilting of $\langle\tilde{\boldsymbol{\omega}}\rangle_t$ via mean-flow gradients, and gains/losses to $\langle\tilde{\boldsymbol{\omega}}\rangle_t$ via spatial heterogeneity of $\mathbf{T}$ (so called turbulent torque). The former and latter are also referred to as Prandtl's secondary flow of the first and second kind [72,73], respectively. The analysis from Secs. IV A to IV C demonstrates that (a) there is flow channeling within the interdune space, and (b) this channeling flow stretches hairpin vortices downwind, enabling gains in streamwise vorticity. Thus, in this section,

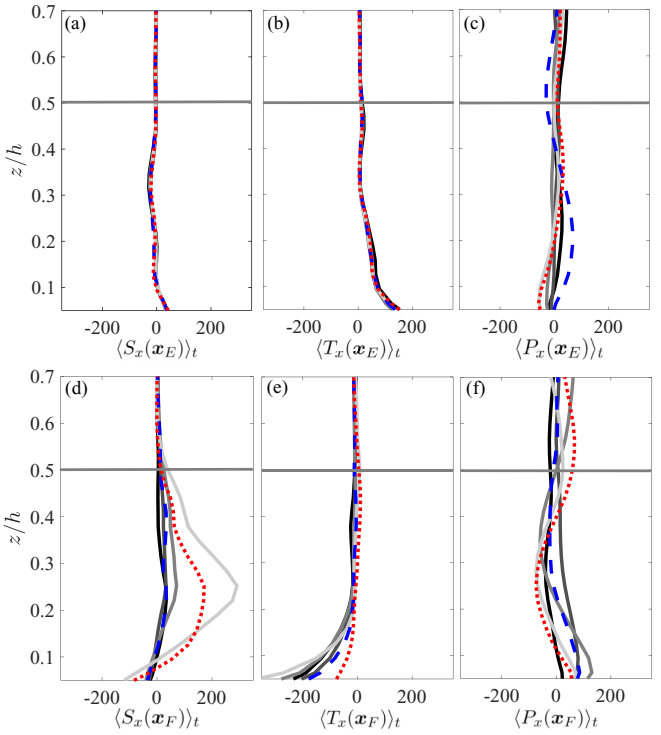

FIG. 9. Vertical profiles of constituent right-hand side terms from Reynolds-averaged streamwise vorticity transport Equation [Eq. (9)], including vortex stretching $\langle S_x\rangle_t$ (a,d), vortex tilting $\langle T_x\rangle_t$ (b,e) and turbulent torque $\langle P_x\rangle_t$(c,f) at discrete streamwise-spanwise locations collocated with Point $\boldsymbol{x}_E$ (a, b, c) and Point $\boldsymbol{x}_F$ (d, e, f) (see also Fig. 2). Black, dark gray, gray, and light gray lines correspond with Cases S1, S2, S3, and S4, respectively, while dashed blue and dotted red lines correspond with S3′ and S4′, respectively. Horizontal gray line denotes small dune height.

we will consider only the x component of Eq. (8):

$$\underbrace{\langle\tilde{\boldsymbol{u}}\rangle_t\cdot\boldsymbol{\nabla}\langle\tilde{\omega}_x\rangle_t}_{\text{Advection}}=\underbrace{\langle\tilde{\omega}_x\rangle_t\partial_x\langle\tilde{u}\rangle_t}_{\text{Stretching, }\langle S_x(\boldsymbol{x})\rangle_t}+\underbrace{\langle\tilde{\omega}_y\rangle_t\partial_y\langle\tilde{u}\rangle_t+\langle\tilde{\omega}_z\rangle_t\partial_z\langle\tilde{u}\rangle_t}_{\text{Tilting, }\langle T_x(\boldsymbol{x})\rangle_t}-\underbrace{\epsilon_{xqi}\partial_q\partial_j\langle\mathsf{T}_{ij}\rangle_t}_{\text{Turbulent torque, }\langle P_x(\boldsymbol{x})\rangle_t}. \tag{9}$$

The symbolic annotations beneath each term in Eq. (9) will be used later to explain mechanisms driving gains and losses to $\langle\tilde{\omega}_x\rangle_t$. It is apparent, from inspection, that the first right-hand side term corresponds with stretching of $\langle\tilde{\omega}_x\rangle_t$, while the second right-hand side term corresponds with tilting of $\langle\tilde{\omega}_y\rangle_t$ and $\langle\tilde{\omega}_z\rangle_t$ into the x direction (note that the sum of these terms was referred to as $\langle P_x(\boldsymbol{x})\rangle_t$ by Perkins [72]).

In Fig. 9, we show vertical profiles of the stretching, tilting, and turbulent torque terms in Eq. (9), at discrete locations $\boldsymbol{x}_E$ and $\boldsymbol{x}_F$, respectively. As shown in Fig. 2, $\boldsymbol{x}_E$ and $\boldsymbol{x}_F$ are at equal streamwise positions, but from outside and within the interdune space, respectively. Thus, differences in the profiles of constituent terms in Eq. (9) at these locations can be attributed to asymmetries associated with the channeling flow, etc. At location $\boldsymbol{x}_E$, Figs. 9(a)–9(c) shows that the profiles for different dune configurations do not exhibit dramatic differences, even as the geometry changes. We see,

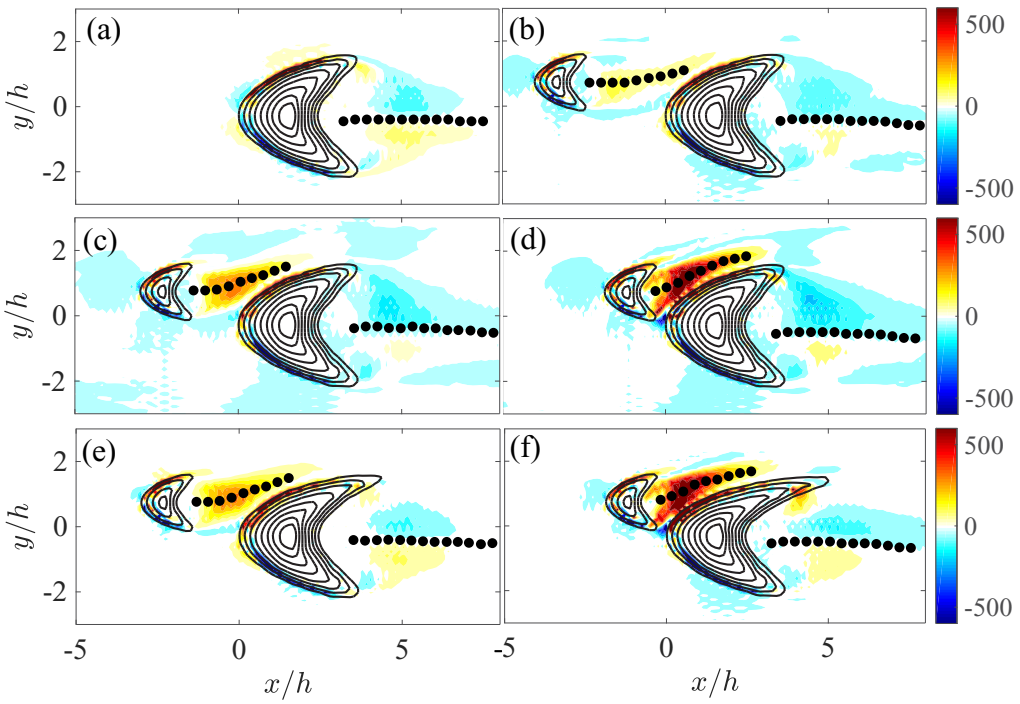

FIG. 10. Color flood contour of Reynolds-averaged term responsible for stretching of streamwise vorticity, $\langle S_x \rangle_t(x, y, z/h = 0.25)$ [see also Eq. (9)]. Panels (a)–(f) correspond with Cases S1, S2, S3, S4, S3′, and S4′, respectively. Included on the color floods are low-pass filtered datapoints for the wake, emanating from the small and large dunes, $\delta_s(x_s; z/h = 0.25)$ and $\delta_l(x_l; z/h = 0.25)$, respectively.

too, that turbulent torque [Fig. 9(c)] makes the dominant contribution to gains and losses in Reynolds-averaged streamwise vorticity. Vortex stretching [Fig. 9(a)] and tilting [Fig. 9(b)] makes a relatively modest contribution, relative to turbulent torque. At location $\boldsymbol{x}_F$, however, the picture changes dramatically, to sustain the interdune roller and channeling flow.

Figures 9(d)–9(f) show the right-hand side terms of Eq. (9), at location $\boldsymbol{x}_F$. It is clear, now, that the upflow dune entirely changes flow processes in the interdune space. Relative to $\boldsymbol{x}_E$, the magnitudes of constituent terms are all higher. It is clear, too, that the largest contribution is derived from the stretching term [Fig. 9(d)]. The peak occurs around $z/h = 0.25$ for Case S4 (light gray) and Case S4′ (dotted red line), which is the signature of flow channeling (stretching) of streamwise vorticity. The magnitude of turbulent torque at $\boldsymbol{x}_F$ exceeds the values reported at $\boldsymbol{x}_E$, but is still small relative to the contribution from stretching.

Figure 9 was used to conclude that stretching provides the largest gain to sustenance of the interdune roller, although this argument was predicated only upon a profile from a discrete location. To further the argument, we have prepared Fig. 10: a horizontal contour of the stretching term, with the wake profiles from Fig. 4 superimposed for generality. For the isolated case [Fig. 10(a)], the magnitude of the stretching term is equal and opposite on the dune stoss face, and the wake exhibits no veering. With introduction of the upflow dune, however, an additional location of stretching is introduced [Figs. 10(b) to 10(f)], and the magnitude of this grows monotonically as spacing decreases [Figs. 10(b) to 10(d)].

V. CONCLUSION

For this work, we used LES to model turbulent high-Reynolds number flow over a series of dune field configurations. The configurations were selected to capture instantaneous realizations of the so-called offset merger interaction, wherein a smaller upflow dune approaches a larger downflow dune. Flume observations have revealed that during advancement of this interaction, the large dune morphology develops a pronounced asymmetry: the horn that is streamwise aligned with the path of the upflow dune exhibits a relatively larger downflow elongation (Fig. 1). To capture the aero- and hydrodynamic processes responsible for this interaction, two of the configurations featured downflow dunes with significant asymmetry (S3′ and S4′).

We showed how the wake profiles of the individual dunes varies with spatial attributes of the configuration, and we showed that the extent of Reynolds-averaged flow asymmetry *declines* for cases in which the large dune is asymmetric. Since the asymmetric dunes feature a larger surface area over which momentum fluxes (drag) can occur, the asymmetry serves to attenuate large mean-flow gradients in the interdune space.

Q criterion was used to highlight the vortical nature of flow around the dunes, which demonstrated the presence of a persistent interdune roller. Shedding of hairpin vortices was ostensible in the conditionally averaged and instantaneous flow. We showed that the dunes impart a distinct energetic peak in the global wavelet power spectrum, accomplished by convolving the input time series of streamwise velocity

fluctuations with a spectrum of wavelet functions, and we related this to the high-Reynolds number Strouhal number. This result was used to provide a cursory estimate for the streamwise spacing between successive rollers, which agreed well with visualizations of vortex cores emanating from the dune crests.

To reconcile preceding findings, we showed contours of differential helicity, since the absence of helicity would indicate an "in place" roller. However, the silhouette of helicity isosurfaces were virtually identical to those of Q criterion, demonstrating that the interdune roller is undergoing persistent migration through the interdune space. This result confirmed, then, that erosion of the large dune is driven by two complementary mechanisms: (1) the interdune roller scours sediment laterally from the large dune; and (2) channeling flow drives saltating grains through the interdune space, with saltation mass flux declining as the interdune channeling flow attenuates.

Given the morphodynamic importance of the interdune roller, we performed a detailed vorticity dynamics analysis to elucidate terms responsible for its sustenance. At these very high Reynolds numbers, vorticity gains and losses occur in response to the stretching and tilting effects, and via spatial heterogeneity of the Reynolds stresses. We considered terms responsible for sustenance of streamwise vorticity, since the roller was closely aligned with this direction. The results show that stretching makes the largest contribution to sustenance of the roller, which is thoroughly consistent with arguments throughout the article on the importance of the interdune roller. A structural model to summarize this process was presented.

Results herein suggest that coherent flow structures within the interdune space—critical to the spatial distributions of basal stress, but entirely neglected by existing flow descriptions based only on surface slope [65,74]—are important in shaping the spatial complexity of natural dunes. Indeed, the results show that the dunes themselves induce flow patterns that sustain flow structures, confounding slope-based descriptions. The application considered herein, the offset-merger interaction, was selected for its convenience and due to prior flume work, although the results have conceptual transcendence to other dune interactions: that is, the flow patterns associated with each dune are persistent over very large distances, and the interaction between such flow patterns can produce nonobvious structures (i.e., the interdune roller, as is the case for the offset-interaction merger).

ACKNOWLEDGMENTS

This work was supported by the National Science Foundation, Grant No. CBET-1603254. Scientific computing resources were provided by the Texas Advanced Computing Center at the University of Texas at Austin. We thank Kalyan Shrestha, UT Dallas, for generously sharing a MatLab visualization script used to create three-dimensional isosurfaces of flow quantities. We thank Ken Christensen, Notre Dame, for providing the barchan dune DEMs used to create the dune configurations considered for this work.

[1] R. Bagnold, *The Physics of Blown Sand and Desert Dunes* (Chapman and Hall, London, 1956).
[2] I. Livingstone, G. Wiggs, and C. Weaver, Earth-Sci. Rev. **80**, 239 (2006).
[3] A. Frank and G. Kocurek, Geomorphology **17**, 47 (1996).
[4] J. Best, J. Geophys. Res. **110**, F04S02 (2005).
[5] J. Best, Fluvial Sedimentol. VII **35**, 41 (2005).
[6] J. Fröhlich, C. Mellen,, W. Rodi, L. Temmerman, and M. Leschziner, J. Fluid Mech. **526**, 19 (2005).
[7] T. Stoesser, C. Braun, M. Garcia-Villalba, and W. Rodi, J. Hydraul. Eng. **134**, 42 (2008).
[8] Y. Shao, *Physics and Modelling of Wind Erosion* (Springer Verlag, Berlin, 2008), p. 452.
[9] M. Omidyeganeh and U. Piomelli, J. Turbulence **12**, N42 (2011).
[10] M. Omidyeganeh and U. Piomelli, J. Fluid Mech. **721**, 454 (2013).
[11] J. Palmer, R. Mejia-Alvarez, J. Best, and K. Christensen, Exp. Fluids **52**, 809 (2012).
[12] W. Anderson and M. Chamecki, Phys. Rev. E **89**, 013005 (2014).
[13] A. Khosronejad and F. Sotiropoulos, J. Fluid Mech. **753**, 150 (2014).
[14] N. Bristow, G. Blois, J. Best, and K. Christensen, J. Geophys. Res.: Earth Surf. **123** (2018), doi:10.1029/2017JF004553.
[15] N. P. Webb, M. S. Galloza, T. M. Zobeck, and J. E. Herrick, Aeol. Res. **20**, 45 (2016).
[16] A. B. Smith, D. W. Jackson, and J. A. G. Cooper, Geomorphology **278**, 28 (2017).
[17] S. Leonardi, P. Orlandi, R. Smalley, L. Djenidi, and R. Antonia, J. Fluid Mech. **491**, 229 (2003).
[18] J. Jimenez, Annu. Rev. Fluid Mech. **36**, 173 (2004).
[19] P. R. Owen, J. Fluid Mech. **20**, 225 (1964).
[20] J. Kok, E. Parteli, T. Michaels, and D. Karam, Rep. Prog. Phys. **75**, 106901 (2012).
[21] T. Pähtz, J. Kok, and H. Herrmann, New J. Phys. **14**, 043035 (2012).
[22] M. P. Almeida, E. J. Parteli, J. S. Andrade, and H. J. Herrmann, Proc. Natl. Acad. Sci. USA **105**, 6222 (2008).
[23] R. L. Martin and J. F. Kok, Sci. Adv. **3**, e1602569 (2017).
[24] C. Wang, Z. Tang, N. Bristow, G. Blois, K. Christensen, and W. Anderson, Comput. Fluids **158**, 72 (2016).
[25] R. Ewing and G. Kocurek, Geomorphology **114**, 175 (2010).
[26] G. Kocurek and R. Ewing, Geomorphology **72**, 94 (2005).
[27] G. Kocurek, M. Carr, R. Ewing, K. Havholm, Y. Nagar, and A. Singhvi, Sediment. Geol. **197**, 313 (2007).
[28] H. Tsoar, Sedimentology **30**, 567 (1983).
[29] N. Lancaster, Sedimentology **36**, 273 (1989).
[30] P. Hersen, K. H. Andersen, H. Elbelrhiti, B. Andreotti, P. Claudin, and S. Douady, Phys. Rev. E **69**, 011304 (2004).
[31] P. Hersen and S. Douady, Geophys. Res. Lett. **32**, L21403 (2005).
[32] E. J. Parteli, O. Durán, M. C. Bourke, H. Tsoar, T. Pöschel, and H. Herrmann, Aeol. Res. **12**, 121 (2014).

[33] B. Werner, Geology **23**, 1107 (1995).
[34] B. Andreotti, P. Claudin, and S. Douady, Eur. Phys. J. B **28**, 321 (2002).
[35] B. Andreotti, P. Claudin, and S. Douady, Eur. Phys. J. B **28**, 341 (2002).
[36] B. Andreotti, J. Fluid Mech. **510**, 47 (2004).
[37] B. Andreotti, A. Fourriere, F. Ould-Kaddour, B. Murray, and P. Claudin, Nature **457**, 1120 (2009).
[38] O. Durán, E. J. Parteli, and H. J. Herrmann, Earth Surf. Processes Landforms **35**, 1591 (2010).
[39] E. M. Franklin and F. Charru, J. Fluid Mech. **675**, 199 (2011).
[40] J. G. Venditti, M. Church, and S. J. Bennett, Sedimentology **52**, 1343 (2005).
[41] J. G. Venditti, M. Church, and S. J. Bennett, Water Resour. Res. **41**, W10423 (2005).
[42] J. G. Venditti, M. A. Church, and S. J. Bennett, J. Geophys. Res.: Earth Surf. **110**, F01009 (2005).
[43] J. G. Venditti, M. Church, and S. J. Bennett, Water Resour. Res. **42**, W07423 (2006).
[44] P. Ortiz and P. K. Smolarkiewicz, Phys. Rev. E **79**, 041307 (2009).
[45] C. Meneveau and J. Katz, Annu. Rev. Fluid Mech. **32**, 1 (2000).
[46] J. Albertson and M. Parlange, Water Resour. Res. **35**, 2121 (1999).
[47] W. Anderson and C. Meneveau, Boundary-Layer Meteorol. **137**, 397 (2010).
[48] W. Anderson, Int. J. Numer. Methods Fluids **71**, 1588 (2012).
[49] U. Piomelli and E. Balaras, Annu. Rev. Fluid Mech. **34**, 349 (2002).
[50] M. Germano, J. Fluid Mech. **238**, 325 (1992).
[51] M. Germano, U. Piomelli, P. Moin, and W. Cabot, Phys. Fluids A **3**, 1760 (1991).
[52] E. Bou-Zeid, C. Meneveau, and M. Parlange, Phys. Fluids **17**, 025105 (2005).
[53] R. Mittal and G. Iaccarino, Annu. Rev. Fluid Mech. **37**, 239 (2005).
[54] W. Anderson, Q. Li, and E. Bou-Zeid, J. Turbulence **16**, 809 (2015).
[55] W. Anderson, J. Fluid Mech. **789**, 567 (2016).
[56] Y. Wu and K. T. Christensen, J. Fluid Mech. **655**, 380 (2010).
[57] R. Antonia, Annu. Rev. Fluid Mech. **13**, 131 (1981).
[58] J. Kim, P. Moin, and R. Moser, J. Fluid Mech. **177**, 133 (1987).
[59] R. Adrian, in *Zoran P. Zaric Memorial International Seminar on Near-Wall Turbulence* (Hemisphere, London, 1988).
[60] J. Sheng, E. Malkiel, and J. Katz, J. Fluid Mech. **633**, 17 (2009).
[61] J. Finnigan, R. Shaw, and E. Patton, J. Fluid Mech. **637**, 387 (2009).
[62] N. Hutchins, J. Monty, B. Ganapathisubramani, H. Ng, and I. Marusic, J. Fluid Mech. **673**, 255 (2011).
[63] D. Richter and P. Sullivan, Phys. Fluids **26**, 103304 (2014).
[64] C. Jacob and W. Anderson, Boundary-Layer Meteorol. **162**, 21 (2016).
[65] P. Jackson and J. Hunt, Q. J. R. Meteorol. Soc. **101**, 929 (1975).
[66] J. Jeong and F. Hussain, J. Fluid Mech. **285**, 69 (1995).
[67] K. Christensen and R. Adrian, J. Fluid Mech. **431**, 433 (2001).
[68] R. Adrian, Phys. Fluids **19**, 041301 (2007).
[69] L. Cohen, Proc IEEE **77**, 941 (1989).
[70] M. Farge, Annu. Rev. Fluid Mech. **24**, 395 (1992).
[71] M. Omidyeganeh, U. Piomelli, K. T. Christensen, and J. L. Best, J. Geophys. Res.: Earth Surf. **118**, 2089 (2013).
[72] H. Perkins, J. Fluid Mech. **44**, 721 (1970).
[73] P. Bradshaw, Annu. Rev. Fluid Mech. **19**, 53 (1987).
[74] X. Gao, C. Narteau, and O. Rozier, J. Geophys. Res.-Earth Surf. **120**, 2200 (2015).